

Research Article

Improvement of the Efficiency of the Axial-Flow Pump at Part Loads due to Installing Outlet Guide Vanes Mechanism

Fan Yang, Hao-ru Zhao, and Chao Liu

School of Hydraulic, Energy and Power Engineering, Yangzhou University, Jiangsu, China

Correspondence should be addressed to Fan Yang; sqzyangfan@126.com

Received 12 September 2015; Accepted 6 December 2015

Academic Editor: Giuseppe Vairo

Copyright © 2016 Fan Yang et al. This is an open access article distributed under the Creative Commons Attribution License, which permits unrestricted use, distribution, and reproduction in any medium, provided the original work is properly cited.

In order to investigate the influence of adjustable outlet guide vane on the hydraulic performance of axial-flow pump at part loads, the axial-flow pump with 7 different outlet guide vane adjustable angles was simulated based on the RNG $k-\varepsilon$ turbulent model and Reynolds time-averaged equations. The Vector graphs of airfoil flow were analyzed in the different operating conditions for different adjustable angles of guide vane. BP-ANN prediction model was established about the effect of adjustable outlet guide vane on the hydraulic performance of axial-flow pump based on the numerical results. The effectiveness of prediction model was verified by theoretical analysis and numerical simulation. The results show that, with the adjustable angle of guide vane increasing along clockwise, the high efficiency area moves to the large flow rate direction; otherwise, that moves to the small flow rate direction. The internal flow field of guide vane is improved by adjusting angle, and the flow separation of tail and guide vane inlet ledge are decreased or eliminated, so that the hydraulic efficiency of pumping system will be improved. The prediction accuracy of BP-ANN model is 1%, which can meet the requirement of practical engineering.

1. Introduction

With the increasing application of an axial-flow pump, the improvement of its efficiency continues to become more and more important. One of the most useful methods to increase its efficiency is the installation of a guide vane behind the pump impeller [1]. Out guide vane (OGV) can improve the head and the efficiency of the pump by transforming the kinetic energy of the rotating flow, which has a tangential velocity component, into pressure energy. When the axial-flow pump is working under off-design condition, the attack angle, which causes hydraulic loss, will always exist at the leading edge of the guide vane. This is because the traditional guide vane is fixed on the guide vane hub with a fixed angle for the design condition and cannot be adjustable with the change in working conditions. The literature on OGV investigations for aircraft engine mainly falls into the following categories: effects of OGV on aircraft engine's noise [2–4], unsteady interaction between the stationary OGVs and the rotor [5], and flow characteristics of OGVs [6–9].

The flow in a compressor OGV blade row downstream of a single-state rotor was carried out by Carrotte et al. [10]. Many researchers studied the internal flow characteristics of OGV based on the whole passage of pump [11–14]. Compared with aircraft engine and compressor, the usage of adjustable OGVs is extremely rare for axial-flow pump. The paper investigates the influence of OGVs setting angles on the hydraulic performance of axial-flow pump by CFD. The internal flow of OGVs is analyzed in different setting angles. The BP-ANN prediction model will be built about the influence of OGVs setting angles on the pump performance based on the resulting data.

2. Numerical Calculations

2.1. Numerical Model and Calculation Method. The numerical model and method for simulating the flow field in the axial-flow pump can be found in previous work by Yang and Liu [15] and Jafarzadeh et al. [16]. The governing equations for the turbulent incompressible flow encountered

in this research are the steady-state RANS equations for the conservation of mass and momentum, given as

$$\frac{\partial}{\partial x_i} (\rho \bar{u}_i) = 0, \quad (1)$$

$$\frac{\partial}{\partial x_i} (\rho \bar{u}_i \bar{u}_j) = -\frac{\partial \bar{p}}{\partial x_i} + \frac{\partial}{\partial x_i} \left(\mu \frac{\partial \bar{u}_i}{\partial x_j} - \overline{\rho u'_i u'_j} \right), \quad (2)$$

where \bar{p} is the averaged pressure, μ is the molecular viscosity, and $-\overline{\rho u'_i u'_j}$ is the Reynolds stress. To correctly account for turbulence, the Reynolds stresses are modeled in order to achieve the closure of (2). The modeling is based on the Boussinesq hypothesis to relate the Reynolds stresses to the mean velocity gradients within the flow. The Reynolds stresses are given by

$$-\overline{\rho u'_i u'_j} = \mu_t \left(\frac{\partial \bar{u}_i}{\partial x_j} + \frac{\partial \bar{u}_j}{\partial x_i} \right) - \frac{2}{3} \delta_{ij} \cdot \left(\rho k + \mu_t \frac{\partial \bar{u}_i}{\partial x_i} \right), \quad (3)$$

where μ_t is the turbulent viscosity and k is the turbulent kinetic energy.

The renormalization group (RNG) k - ε turbulent model is widely applied in turbo machines, which is suitable for simulating the complex flow in rotating and high curvature computational domain. A more comprehensive description of RNG theory and its applications to turbulence computation can be found in [17].

The turbulence kinetic energy k and its rate dissipation ε are obtained from the following transport equations:

$$\frac{\partial (\rho k \bar{u}_i)}{\partial x_i} = \frac{\partial}{\partial x_j} \left(\alpha_k \mu_{\text{eff}} \frac{\partial k}{\partial x_j} \right) + G_k - \rho \varepsilon, \quad (4)$$

$$\frac{\partial (\rho \varepsilon \bar{u}_i)}{\partial x_i} = \frac{\partial}{\partial x_j} \left(\alpha_\varepsilon \mu_{\text{eff}} \frac{\partial \varepsilon}{\partial x_j} \right) + \frac{C_{1\varepsilon}^*}{k} G_k - C_{2\varepsilon} \rho \frac{\varepsilon^2}{k}. \quad (5)$$

The production term in (4) is given by

$$G_k = \mu_t S^2, \quad (6)$$

where S is the modulus of the mean rate-of-strain tensor, defined by

$$S = \sqrt{2S_{ij}S_{ij}}, \quad S_{ij} = \frac{1}{2} \left(\frac{\partial \bar{u}_i}{\partial x_j} + \frac{\partial \bar{u}_j}{\partial x_i} \right). \quad (7)$$

The effective viscosity is calculated by

$$\mu_{\text{eff}} = \mu + \mu_t, \quad \mu_t = \rho C_\mu \frac{k^2}{\varepsilon}, \quad (8)$$

with $C_\mu = 0.0845$, $\alpha_k = \alpha_\varepsilon = 1.39$, $C_{1\varepsilon} = 1.42$, and

$$C_{1\varepsilon}^* = C_{1\varepsilon} - \frac{\eta(1-\eta/\eta_0)}{1+\beta\eta^3}, \quad (9)$$

$$\eta = (2S_{ij} \cdot S_{ij})^{0.5} \frac{k}{\varepsilon}, \quad \eta_0 = 4.377, \quad \beta = 0.012, \quad C_{2\varepsilon} = 1.68.$$

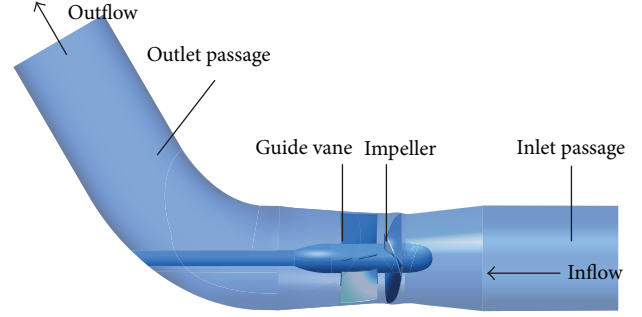


FIGURE 1: The whole flow passage axial-flow pump model.

In the present calculation work, the commercial CFD code ANSYS CFX14.0 is employed. ANSYS CFX uses the element based finite volume method and an algebraic multigrid approach. The equations solved in the calculation are the Navier-Stokes equations coupled with the RNG k - ε turbulence model. A uniform axial velocity based on the mass-flow rate is specified at the inlet for each computation run, and the static pressure at the outlet is set to 1.2 atm. The turbulence intensity at the inlet totally depends on the upstream history of flow. Since the fluid in the suction tank is undisturbed, the turbulence intensity for all conditions is considered 1%. Scalable wall functions are used to simulate the boundary layers. Adiabatic and hydraulically smooth walls with no slip condition were considered at solid boundaries. Periodic boundaries are set at the blade passage interfaces. Water was used as a working fluid in ambient condition.

2.2. Computational Domain and Mesh. Figure 1 shows 3D geometry of axial-flow pump model, with the specific speed n_s of 1200 and impeller diameter of 300 mm, which is used to simulate and measure its entire flow field. The specific speed n_s is defined below:

$$n_s = \frac{3.65n\sqrt{Q}}{H^{3/4}} = 3.65 \left(\frac{\text{r/min} \cdot (\text{m}^3/\text{s})^{1/2}}{\text{m}^{3/4}} \right). \quad (10)$$

The impeller has 3 blades and the outlet guide vane has 5 blades. The rotating speed n is 1450 r/min. The average tip clearance of impeller is 0.2 mm at blade angle $\varphi = 0^\circ$, which are the same as those of the experimental model. The computational domain is the flow passage from the inlet to outlet, including the inlet passage, outlet passage, impeller, and guide vane.

The grid quality in the impeller and guide vane will affect the accuracy of axial-flow pump simulation. Accordingly, H/J/L-type topology structure is applied to the impeller, and H-type topology structure is applied to the outlet guide vane. O-type grid is used at the blade surface region to control boundary layer distribution. Prior to step for analysis of axial-flow pump, in order to determine the optimal number of grids, a preliminary grid dependency test with numbers of nodes ranging from 500000 to 1600000 is carried out. The computations have shown that grid convergence has been obtained for the performance of the axial-flow pump

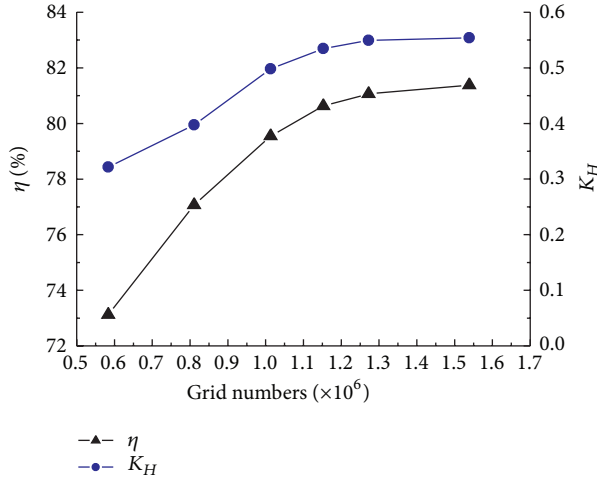


FIGURE 2: Verification of grid independence to prediction of performances.

at $K_Q = 0.521$, as shown in Figure 2. With the increase of grid numbers, the head coefficient K_H and efficiency change greatly at first and then change very little gradually. Finally, the appropriate grid number for the simulation was determined by the preliminary simulation results. In the present study, grid number 1272707 was selected for the final simulation.

The nondimensional head and power coefficients are defined as follows.

Head coefficient is as follows:

$$K_H = \frac{gH}{n^2 D^2}, \quad (11)$$

where K_H is head coefficient, H is the head of the axial-flow pump, n is rotation speed, and D is the impeller diameter.

Flow coefficient is as follows:

$$K_Q = \frac{Q}{nD^3}, \quad (12)$$

where the efficiency of the pump is defined as follows:

$$\eta = \frac{30\rho gQH}{\pi nM} \times 100, \quad (13)$$

where Q is volume flow rate and M is the measured torque.

3. Performance Prediction Results and Experimental Validation

3.1. Test Device and Method. Physical model of axial-flow pump was tested in the Hydrodynamic Engineering Laboratory of Jiangsu Province. Figure 3 shows the rig for the experimental measurements. The test apparatus consists of three sections: ① water supply section: the inlet water tank, the outlet water tank, the surge water tank, mixed-flow pump, and regulating valve; ② outlet section: pressure gauge, electromagnetic flowmeter, and regulating valve; and ③ pump section: axial-flow pump, composite torque detector,

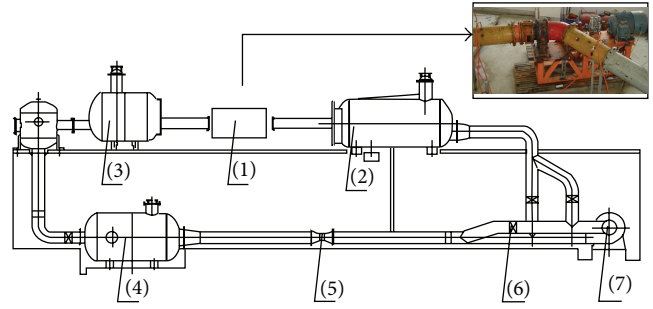


FIGURE 3: Schematic diagram of the experimental rig: (1) axial-flow pump, (2) inlet water tank, (3) outlet water tank, (4) surge water tank, (5) electromagnetic flowmeter, (6) regulating valve, and (7) mixed-flow pump.

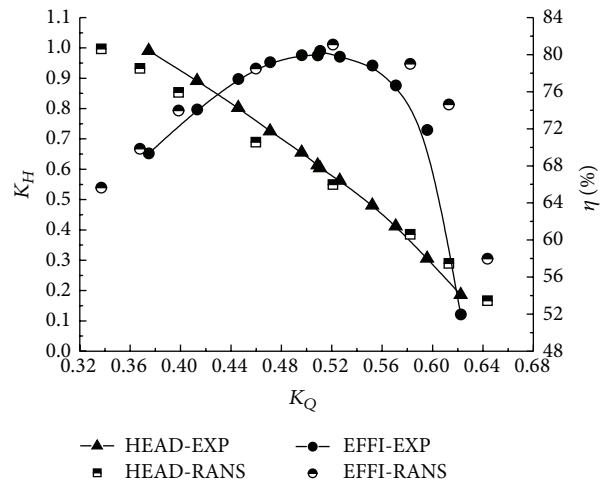


FIGURE 4: Experimental and calculated results.

and motor. Axial-flow pump head is measured by differential pressure transmitter EJA110A with $\pm 0.113\%$, and measuring sections are closed in the tanks with the inlet and outlet passages for concluding hydraulic loss of inlet and outlet sections. Torque is measured by TS-3100B digital torque and speed sensor with $\pm 0.0203\%$, which is transmitted by pump shaft. Flow rate is measured by E-mag DN400 electromagnetic flowmeter with $\pm 0.197\%$.

3.2. Results Comparison. According to test data, the highest efficiency of axial-flow pump is 80.39% at blade angle $\varphi = 0^\circ$, with flow rate coefficient K_Q of 0.511 and head coefficient K_H of 0.604. The prediction data agree with the experimental head and efficiency, as shown in Figure 4. There is a good quantitative agreement at the flow rate coefficient K_Q of 0.36~0.60, with the maximum relative errors smaller than 4.0%, which demonstrates that numerical calculations simulate the pump performance accurately.

4. Results and Discussion

4.1. Influence of OGV on the Hydraulic Performance of Axial-Flow Pump. The hydraulic performances of axial-flow pump

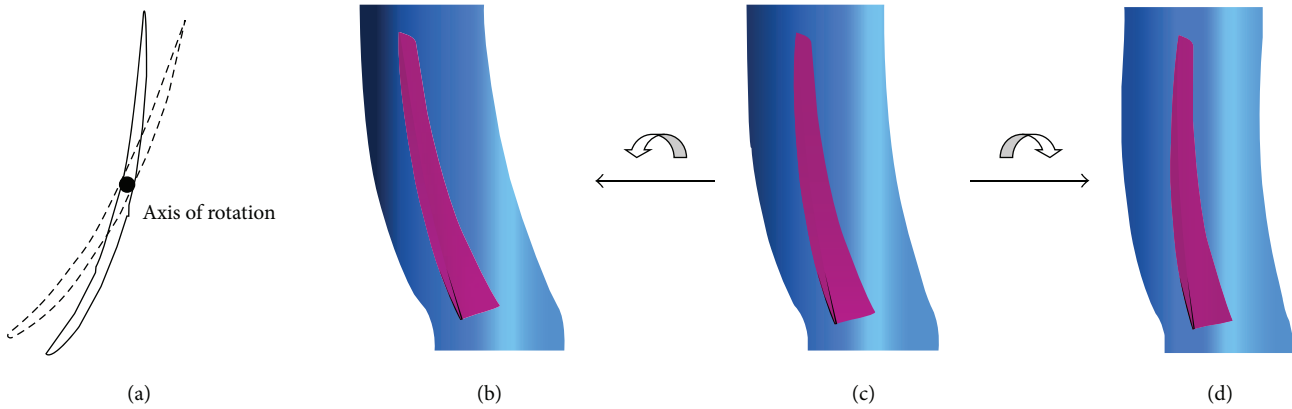


FIGURE 5: Schematic diagram of (a) OGV adjustment and different OGV setting angles: (b) OGV -5° , (c) OGV 0° , and (d) OGV 5° .

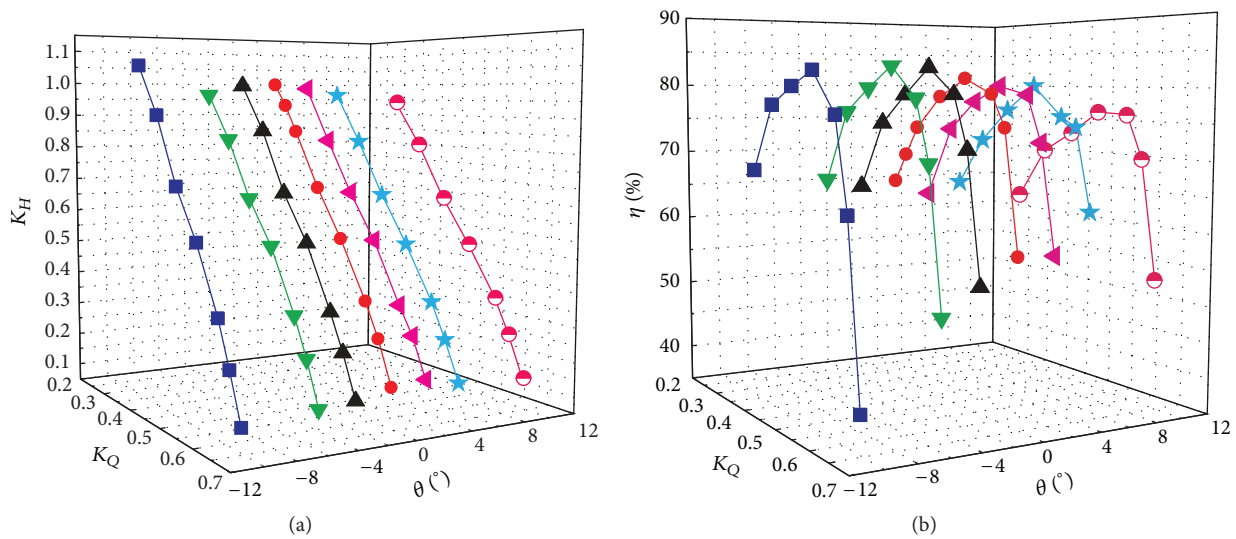


FIGURE 6: Performance curves of (a) pump head coefficient K_H and (b) efficiency for different flow rate coefficient K_Q and OGVs setting angles θ .

with seven different OGV setting angles were predicted. The OGV setting angle is in the range of $-10^\circ \sim +10^\circ$. The 3D models of OGV with three different setting angles are shown in Figure 5.

The hydraulic performances of axial-flow pump with seven different OGV setting angles were predicted. The OGV setting angle is in the range of $-10^\circ \sim +10^\circ$. Figure 6 shows the numerical results of pump head coefficient K_H and efficiency for different flow rates. The change law of pump efficiency, head coefficient K_H , and OGV setting angle is not the same in the same flow rate coefficient K_Q . The OGV setting angle has great influence on the inner flow pattern of OGV and hydraulic performance of pump, and the rotor-stator interaction is complex. The OGV setting angle has great influence on the hydraulic performance of outlet passage. When the OGVs are regulated to the positive angle, the hydraulic performance will be improved in the large flow rate condition. When the OGVs are regulated to the negative angle, the hydraulic performance will be improved in the small flow rate condition. If the OGVs are regulated to the

positive angle, the high efficiency area will be closed to the large flow rate condition; otherwise, the high efficiency area will be closed to the small flow rate condition. In order to eliminate the inlet incidence angle and tail flow separation of blade, the OGV setting angle should be regulated according to axial-flow pump operating conditions.

4.2. Internal Flow Pattern of Axial-Flow Pump. The flow patterns in the OGV channel at low flow rate condition ($K_Q = 0.398$), high efficiency flow rate condition ($K_Q = 0.521$), and large flow rate condition ($K_Q = 0.644$) are shown in Figures 7–9. These figures show the flow patterns of OGV channel in different OGV setting angles.

In the low flow rate condition ($K_Q = 0.398$), the vortices appeared in the OGV suction surface from the 1/4 length of inlet edge, the backflow is in the inlet edge of blade, but the flow pattern of trailing edge is good for OGV. The hydraulic loss increases because of vortices appearing, and it is 21.41% of the pump head in $K_Q = 0.398$. With the increase of OGV setting angles to positive, the hydraulic loss increases

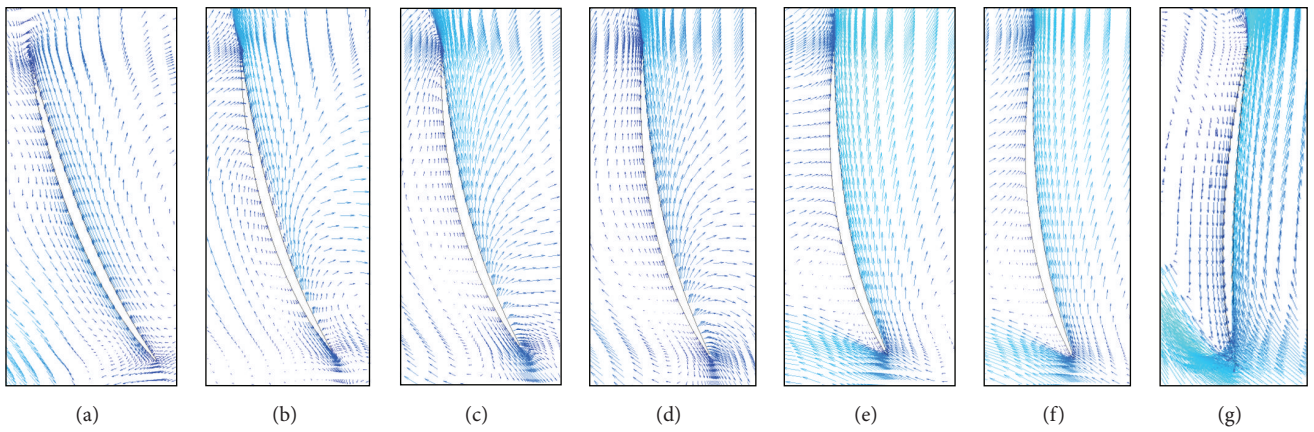


FIGURE 7: Flow pattern of OGV channel at low flow rate condition $K_Q = 0.398$: (a) OGV -10° , (b) OGV -5° , (c) OGV -2.5° , (d) OGV 0° , (e) OGV 2.5° , (f) OGV 5° , and (g) OGV 10° .

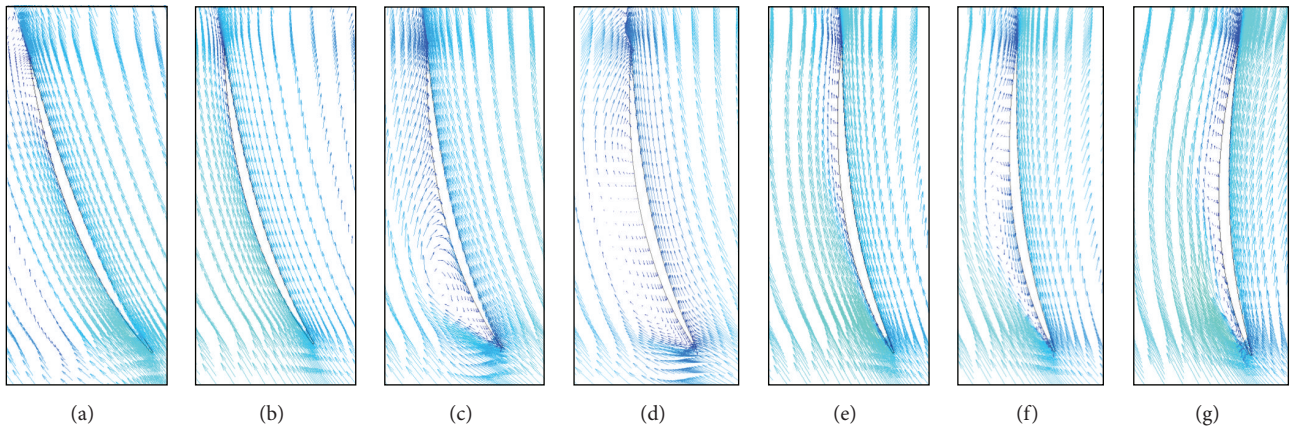


FIGURE 8: Flow pattern of OGV channel at high efficiency flow rate condition $K_Q = 0.521$: (a) OGV -10° , (b) OGV -5° , (c) OGV -2.5° , (d) OGV 0° , (e) OGV 2.5° , (f) OGV 5° , and (g) OGV 10° .

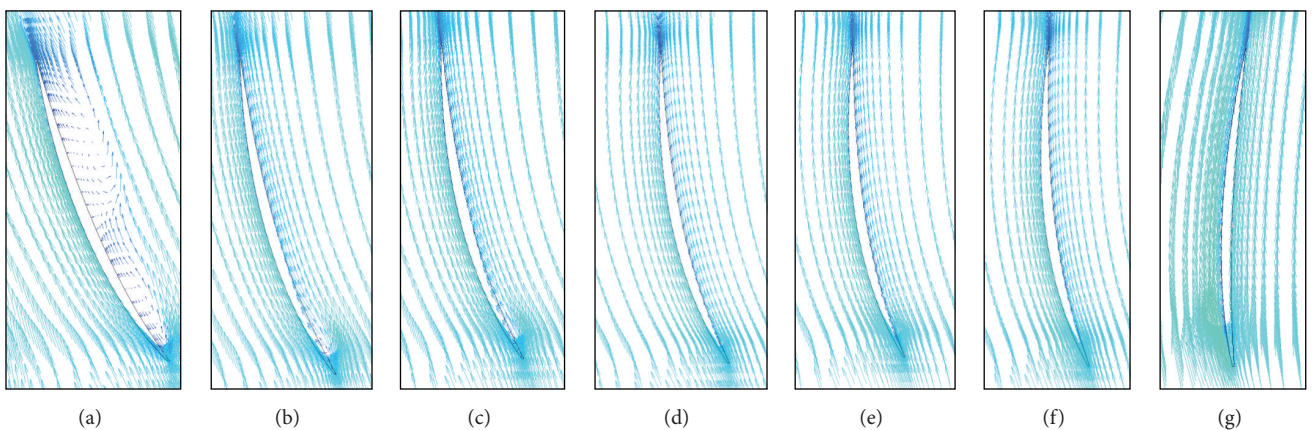


FIGURE 9: Flow pattern of OGV channel at large flow rate condition $K_Q = 0.644$: (a) OGV -10° , (b) OGV -5° , (c) OGV -2.5° , (d) OGV 0° , (e) OGV 2.5° , (f) OGV 5° , and (g) OGV 10° .

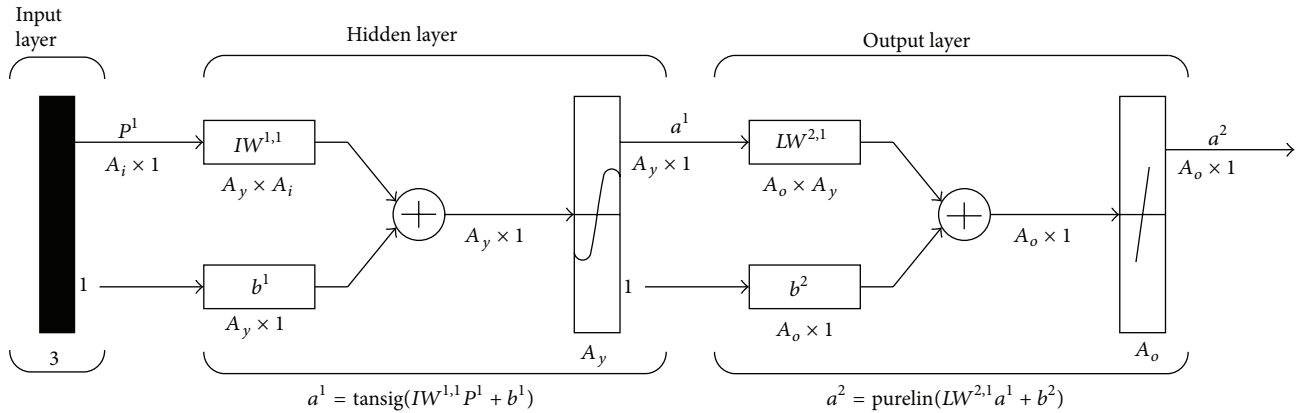


FIGURE 10: Topology structure of BP-ANN network.

gradually. Compared with the OGV setting angle $\theta = 0^\circ$, the hydraulic loss increases by 38.66% and the hydraulic efficiency dropped by 3.93% in the OGV setting angle $\theta = 10^\circ$. From Figure 7, flow separation occurs in the trailing edge of OGV blade, and it influences the flow field of the inlet region of OGV blade. The hydraulic loss increases because the flow hits the pressure surface of OGV blades. With the increase of OGV setting angles to negative, the hydraulic loss decreases firstly and then increases. Compared with the OGV setting angle $\theta = -2.5^\circ$, the hydraulic loss decreases by 6.41% and the hydraulic efficiency improves by 0.74%. With the increase of OGV setting angles to negative from $\theta = -2.5^\circ$, the area of vortex region increases gradually in the OGV suction surface, and the hydraulic loss increases and the hydraulic efficiency decreases gradually. The vortex region accounts approximately for 33.3% of the OGV suction surface area at OGV setting angle $\theta = -2.5^\circ$.

In the high efficiency flow rate condition ($K_Q = 0.521$), the vortices appeared in the OGV suction surface from the 1/2 length of inlet edge, and the hydraulic loss of OGV accounts for 8.22% of axial-flow pump head. Compared with the OGV setting angle $\theta = 0^\circ$, the hydraulic loss of OGV increases approximately by 55%, the hydraulic efficiency of pump decreases approximately by 1% at $\theta = 2.5^\circ$ and $\theta = 5^\circ$, and the hydraulic loss of OGV increases by 118.55%, and the hydraulic efficiency of pump decreases by 4.86% at $\theta = 10^\circ$. The vortex region is in the middle of OGV suction surface at $\theta = 2.5^\circ$ and $\theta = 5^\circ$, and the vortex region extends to the inlet region of OGV blade at $\theta = 10^\circ$ from Figure 8. With the increase of OGV setting angle to negative, the hydraulic loss decreases firstly and then increases. Compared with the OGV setting angle $\theta = 0^\circ$, the hydraulic loss decreases by 14.55% and the hydraulic efficiency improved by 1.59% at $\theta = -5^\circ$. With the increase of OGV setting angle to negative from $\theta = -5^\circ$, the hydraulic loss increases and the hydraulic efficiency decreases gradually. The vortex is in the trailing edge of OGV blade suction surface at $\theta = -10^\circ$. The hydraulic loss increases because flow separation is in the trailing edge of OGV blade.

In the large flow rate condition ($K_Q = 0.644$), with the increase of OGV setting angles to negative, the vortex region increases gradually in the OGV pressure surface. The

hydraulic loss of OGV increases gradually. Compared with the OGV setting angle $\theta = 0^\circ$, the hydraulic loss increases by 297%, and the hydraulic efficiency of pump decreases by 17.87%. From Figure 9, the vortex region is in the OGV pressure surface from the 1/4 and the 3/4 length of inlet edge. The vortex causes the hydraulic efficiency to drop significantly. There are no vortex and flow separation around the airfoil of OGV blades at the OGV setting angles $\theta = 0^\circ$, $\theta = 2.5^\circ$, and $\theta = 5^\circ$. The flow separation is in the trailing edge of OGV blade, so the hydraulic loss increases at $\theta = 10^\circ$. The coupling effects of impeller, OGV, and outlet passage are considered in the numerical simulation of axial-flow pump. Compared with the OGV setting angle $\theta = 0^\circ$, the hydraulic loss decreases by 14.65%, and the hydraulic efficiency of pump improved by 5.29% at the OGV setting angle $\theta = 5^\circ$.

4.3. Artificial Neural Networks. In this paper, a computational tool, known as back propagation artificial neural networks (BP-ANN), is used to predict the hydraulic performance of axial-flow pump with OGVs. The network usually consists of input layer, hidden layer, and output layer. A schematic diagram of the typical three-layer feed-forward neural network architecture is shown in Figure 10. The prediction mathematical model is constructed based on the modified BP-ANN. The modified BP-ANN consists of two layers of back propagation network structure. The hyperbolic tangent S-type function $\text{tansig}()$ is used in the input layer and hidden layer. The pure linear function $\text{purelin}()$ is used in the output layer. The neurons numbers of input layer are assumed as the samples index A_i . The repeated training of node number was carried out in the hidden layer [18], and the node numbers are assumed as A_y . The neurons numbers of output layer are assumed as A_o , so the network structure model is $A_i \times A_y \times A_o$. The BP elastic algorithm $\text{trainrp}()$ was adopted for training function, and it can be used in the bulk mode training. It has fast convergence speed and calculation with small storage space. The topology structure of BP-ANN network is shown in Figure 10.

The impeller torque T_p , the pump flow rate coefficient K_Q , the pump head coefficient K_H , and the OGVs setting angle $\Delta\theta$ are assumed as input variables, the neurons number of

TABLE 1: Parameters of test samples.

Flow rate coefficient K_Q	Input samples		The OGVs setting angles ($^\circ$)	Simulated results (CFD)	Predicted results (BP-ANN)	Deviation/%
	Head coefficient K_H	Torque T_p				
0.337	1.005	119.942	5	65.053	65.255	0.31
0.398	0.824	105.162	5	71.913	71.892	0.03
0.460	0.671	92.795	5	76.527	76.497	0.04
0.521	0.539	80.752	5	80.076	80.043	0.04
0.582	0.365	64.514	5	75.890	76.630	0.98
0.613	0.288	54.436	5	74.546	74.478	0.09
0.644	0.175	41.081	5	63.268	62.661	0.96

input layer is 4 and the neurons number of output layer is 1 for BP-ANN network. The neurons number of hidden layer is calculated by

$$A_y = \sqrt{A_i + A_o} + a, \quad (14)$$

where $1 < a < 10$. The neurons number of hidden layer is 1 by using the comparative method and cut-and-try method. The network structure model is $4 \times 9 \times 1$.

The seven groups of OGVs setting angles were used to train and test the BP-ANN prediction model, and each group includes seven pump operating conditions and 49 groups of pump performance data. The 49 groups were divided into two parts: one part was used as training samples, and the other part was used to exam the BP-ANN prediction model. In order to ensure the learning precision of BP-ANN prediction model, more training samples were needed, 42 groups were chosen randomly, and the rest of data were used to test the prediction model. Normalization processing was carried out for samples firstly, and then the prediction model was trained. Function `premnmx()` was used to recode the normalization processing of input value and output value in Matlab software, so that training samples were in the range of -1 to 1 .

The function `newff()` was used to construct the BP-ANN prediction model by using the commercial mathematical software Matrix & Laboratory; it can be expressed by

$$\begin{aligned} \text{net} \\ = \text{newff}(P, T, S, \text{TF}, \text{BTF}, \text{BLF}, \text{PF}, \text{IPF}, \text{OPF}, \text{DDF}), \end{aligned} \quad (15)$$

where `net` is mesh object of BP-ANN, P is the number of input groups, T is the number of output groups, S is unit number of hidden layers, `TF` is the transfer function of each layer, `BTF` is the training function of BP-ANN, `BLF` is learning function of weight, `PF` is objective performance function, `IPF` is row unit array of input proceeding function, `OPF` is row unit array of output proceeding function, and `DDF` is data decomposition function.

The prediction model was trained by using 42 groups of pump performances data. The trained prediction model has a good stability and satisfies the precision demands for prediction assessment. The error curve is shown in Figure 11.

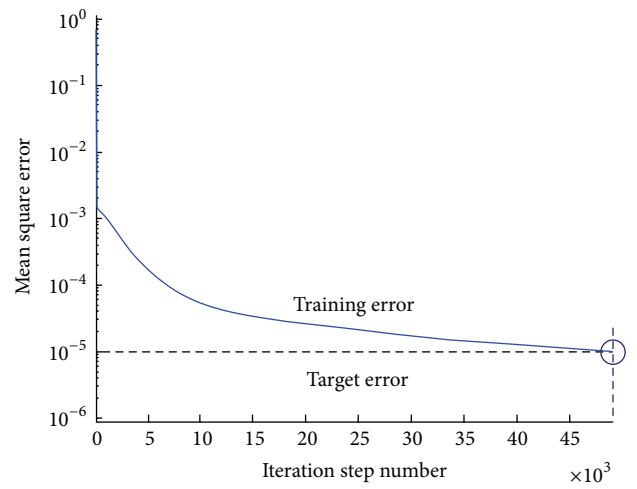


FIGURE 11: Mean squared error curve of the network.

In order to validate the effectiveness of prediction model, numerical results of 7 operating conditions were assumed as testing sample at the OGVs setting angle $\theta = 5^\circ$. The comparison of predicted results and simulated results is shown in Table 1. The maximum deviation is 0.98%, the minimum deviation is 0.03%, and the average deviation is 0.35%. The prediction accuracy of BP-ANN model is below 1%, which can meet the requirement of practical engineering.

The pump performance is predicted by using BP-ANN model, which needs to give 4 parameters, including setting angle, flow rate coefficient, torque, and head coefficient. The functional relation surface of flow rate coefficient K_Q , head coefficient K_H , and the OGVs setting angles θ with a determination coefficient of 0.997, and the functional relation surface of flow rate coefficient K_Q , the OGVs setting angles θ , and torque T_p with a determination coefficient of 0.998 are shown in Figure 12 by using binary nonlinear regression analysis method.

The suitable OGVs setting angle can be predicted firstly according to flow rate coefficient and head coefficient based on the fitting surface of binary nonlinear function about K_Q - K_H - θ ; then, the torque can be predicted according to flow rate coefficient and OGVs setting angle based on the fitting

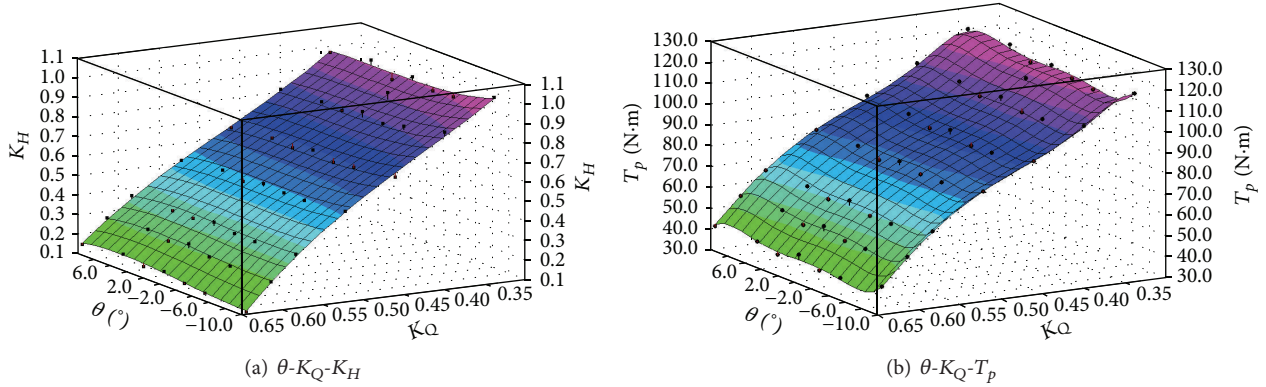


FIGURE 12: Fitting surface of binary nonlinear functions.

surface of binary nonlinear function about K_Q - K_H - T_p , and the pump hydraulic efficiency can be predicted by using BP-ANN model according to different OGVs setting angles.

As shown in Figure 13, if the guide vane inlet attack angle $\alpha_j = 0$, the OGVs suitable angle β will be calculated by

$$\begin{aligned} v_{1a} &= \frac{Q}{\pi(R_s^2 - R_h^2)}, \\ \beta &= \arctan \frac{v_{1a}}{k_0 v_{1u}}, \\ k_0 &= 1 - \frac{ZS_{1u}}{\pi D_c}, \end{aligned} \quad (16)$$

where k_0 is the crowding coefficient at the entrance of OGVs, v_{1a} is the axial velocity at the entrance of OGVs, v_{1u} is the circumferential component of absolute velocity at the entrance of OGVs, and S_{1u} is the circulation thickness of blade at the OGVs inlet.

The OGVs suitable angles are intended to maintain the shock free flow pattern. The schematic diagram of OGV is shown in Figure 13. The basic idea of the OGV is that the guide vane inlet flow angle α_j should be adjusted according to the impeller outlet flow angle β_c to reduce hydraulic loss. The impeller outlet flow angle β_c can be derived from the velocity triangle when the blade angle and flow rate are known, as shown in Figure 13. According to theorem of moment of momentum about impeller outlet flow and guide vane inlet flow $v_{1u}R_d = v_{0u}R_y$, if the radius of OGV calculation flow surface is relative to impeller calculation flow surface, v_{1u} will be equal to v_{0u} . The formula of α_c can be derived from the velocity triangle and discharge as follows [19]:

$$\alpha_c = \arctan \left[\frac{60Q}{2\pi^2 (R_c^2 - r_c^2) R_c n - 60Q \cot \beta_c} \right], \quad (17)$$

where R_c is the radius of pump case at the impeller outlet, r_c is the radius of hub at the impeller outlet, and n is the impeller rotation speed.

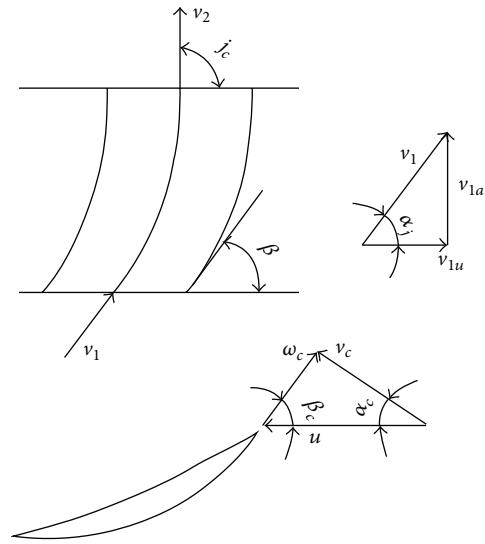


FIGURE 13: Schematic diagram of OGV adjustment.

If the hydraulic loss is minimum, the OGVs suitable angle β will be equal to α_j and α_c . The OGVs suitable angle β can be written as follows:

$$\beta = \arctan \left(\frac{\pi D_c \tan \alpha_c}{\pi D_c - ZS_{1u}} \right); \quad S_{1u} = \frac{S_1}{\sin \beta}, \quad (18)$$

where S_1 is the blade thickness at the impeller inlet.

The OGVs setting angle θ is calculated by

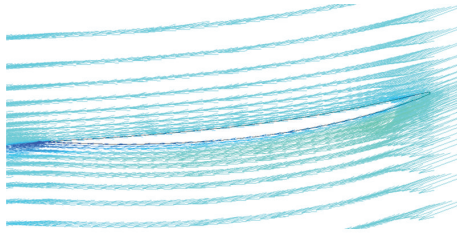
$$\theta = \beta - \beta_d, \quad (19)$$

where β is the OGVs suitable angle and β_d is OGVs fixed angle.

The OGVs setting angle θ can be calculated based on the flow rate coefficient K_Q and head coefficient K_H ; then, the torque T_p is calculated based on the OGVs setting angle θ and the flow rate coefficient K_Q . The three operating conditions ($K_Q = 0.521, 0.552, \text{ and } 0.664$) were chosen for verifying the BP-ANN model. The calculation results are shown in Table 2 based on the OGV fixed angle formula given in [19] and binary nonlinear function.

TABLE 2: Adjustable angles of outlet guide vane and performance of pumping system.

Flow rate coefficient K_Q	Head coefficient K_H	OGV		Setting angles $\theta/(\circ)$	Torque (N-m)	Efficiency/(%)
		Suitable angle $\beta/(\circ)$	Fixed angle $\beta/(\circ)$			
0.521	0.541	59.64	64.8	-5.16	77.825	83.55
0.552	0.458	63.31	64.8	1.49	72.081	80.79
0.664	0.171	68.53	64.8	3.73	40.360	60.96

FIGURE 14: Vector graph of airfoil flow ($K_Q = 0.552$).

The predicted efficiency is closer to calculated efficiency $\eta = 82.67\%$ by CFD at the OGV setting angle $\theta = -5^\circ$, and the absolute deviation is less than 1%. The difference is because the rotor-stator interaction is not considered in the OGV setting angle formulae (17)–(19).

In order to verify the feasibility of predication method, the internal flow of axial-flow pump was simulated by ANSYS CFX at $K_Q = 0.552$ for the OGV setting angle $\theta = 1.49^\circ$. The Vector graph of airfoil flow of OGV is shown in Figure 14. There are no vortex and flow separation around the airfoil. The pump efficiency is 81.12% based on the simulated results; the difference value is 0.41%, compared with predicted results $\eta = 80.79\%$ in Table 2. The pump efficiency $\eta = 83.55\%$, and the OGV setting angle $\theta = -5.16^\circ$ in the flow rate coefficient $K_Q = 0.521$.

5. Conclusion

Simulations of the three-dimensional steady flow in an axial-flow pump with OGV were conducted using the commercial CFD software ANSYS CFX, and the BP-ANN prediction model was established firstly about the effect of adjustable outlet guide vane on the hydraulic performance of axial-flow pump. The results show the following:

- (1) The mathematical model used in this paper can accurately simulate the flow field inside the axial-flow pump. The computational K_Q - K_H curves agree well with the experimental ones.
- (2) The internal flow field of guide vane is improved by adjusting angle, and the flow separation of tail and guide vane inlet ledge are decreased or eliminated, so that the hydraulic efficiency of pumping system will be improved.

- (3) The adjustable outlet guide vane can significantly improve the head and efficiency of the pump at off-design conditions. If the OGVs are regulated to the positive angle, the high efficiency area will be closed to the large flow rate condition; otherwise, the high efficiency area will be closed to the small flow rate condition.

- (4) BP-ANN prediction model is established firstly about the effect of adjustable outlet guide vane on the hydraulic performance of axial-flow pump. The prediction accuracy of BP-ANN model is 1%, which can meet the requirement of practical engineering.

Conflict of Interests

The authors declare that there is no conflict of interests regarding the publication of this paper.

Acknowledgments

This work was supported by the National Natural Science Foundation of China (Grant no. 51376155), the Natural Science Foundation of Jiangsu Province (Grant no. BK20150457), the Natural Science Foundation of Jiangsu Higher Education Institutions of China (Grant no. 14KJB570003), and the Priority Academic Program Development of Jiangsu Higher Education Institutions (PAPD).

References

- [1] B. Nesbitt, *Handbook of Pumps and Pumping*, Elsevier Science & Technology Books, 2006.
- [2] Y. D. Khaletskiy and Y. S. Pochkin, "Fan noise reduction of an aircraft engine by inclining the outlet guide vanes," *Acoustical Physics*, vol. 61, no. 1, pp. 101–108, 2015.
- [3] D. Giacché, L. Xu, and J.-P. Coupland, "Optimization of bypass outlet guide vane for low interaction noise," *AIAA Journal*, vol. 52, no. 6, pp. 1145–1158, 2014.
- [4] X. Sun, Z. Yang, and X. Wang, "Effect of fan outlet guide vane on the acoustic treatment design in aeroengine nacelle," *Journal of Sound and Vibration*, vol. 302, no. 1-2, pp. 287–312, 2007.
- [5] A. R. Wadia, P. N. Szucs, and K. L. Gundy-Burlet, "Design and testing of swept and leaned outlet guide vanes to reduce stator-strut-splitter aerodynamic flow interactions," *Journal of Turbomachinery*, vol. 121, no. 3, pp. 416–427, 1999.
- [6] J. Li, G. Page, and J. McGuirk, "Coupled reynolds-averaged navier-stokes/large-eddy simulation for outlet guide vane and

- prediffuser flows,” *AIAA Journal*, vol. 53, no. 3, pp. 678–691, 2015.
- [7] C. A’Barrow, J. F. Carrotte, A. D. Walker, and A. M. Rolt, “Aerodynamic performance of a coolant flow off-take downstream of an outlet guide vane,” *Journal of Turbomachinery*, vol. 135, no. 1, Article ID 011006, 2012.
- [8] J. Hjärne, J. Larsson, V. Chernoray, and L. Löfdahl, “An experimental investigation of secondary flows and loss development downstream of a highly loaded low pressure turbine outlet guide vane cascade,” in *Proceedings of the ASME Turbo Expo*, pp. 681–690, Barcelona, Spain, May 2006.
- [9] T. Sonoda and H.-A. Schreiber, “Aerodynamic characteristics of supercritical outlet guide vanes at low Reynolds number conditions,” *Journal of Turbomachinery*, vol. 129, no. 4, pp. 694–704, 2007.
- [10] J. F. Carrotte, K. F. Young, and S. J. Stevens, “Measurements of the flow field within a compressor outlet guide vane passage,” *Journal of Turbomachinery*, vol. 117, no. 1, pp. 29–37, 1995.
- [11] F.-P. Tang and G.-Q. Wang, “Influence of outlet guide vanes upon performances of water jet axial-flow pump,” *Journal of Ship Mechanics*, vol. 10, no. 6, pp. 19–26, 2006.
- [12] H. Zhu and R. Zhang, “Numerical analysis on the distribution features of velocity circulation of axial-flow pump,” *Revista Tecnica de la Facultad de Ingenieria Universidad del Zulia*, vol. 37, no. 3, pp. 14–21, 2014.
- [13] D. Kaya, “Experimental study on regaining the tangential velocity energy of axial flow pump,” *Energy Conversion and Management*, vol. 44, no. 11, pp. 1817–1829, 2003.
- [14] H. Zhang, W.-D. Shi, B. Chen, Q.-H. Zhang, and W.-D. Cao, “Experimental study of flow field in interface area between impeller and guide vane of axial flow pump,” *Journal of Hydrodynamics*, vol. 26, no. 6, pp. 894–901, 2015.
- [15] F. Yang and C. Liu, “Pressure pulsations of the blade region in S-shaped shaft-extension tubular pumping system,” *Mathematical Problems in Engineering*, vol. 2014, Article ID 820135, 10 pages, 2014.
- [16] B. Jafarzadeh, A. Hajari, M. M. Alishahi, and M. H. Akbari, “The flow simulation of a low-specific-speed high-speed centrifugal pump,” *Applied Mathematical Modelling*, vol. 35, no. 1, pp. 242–249, 2011.
- [17] V. Yakhot and S. A. Orszag, “Renormalization group analysis of turbulence. I. Basic theory,” *Journal of Scientific Computing*, vol. 1, no. 1, pp. 3–51, 1986.
- [18] S. Rajakarunakaran, P. Venkumar, D. Devaraj, and K. S. P. Rao, “Artificial neural network approach for fault detection in rotary system,” *Applied Soft Computing Journal*, vol. 8, no. 1, pp. 740–748, 2008.
- [19] Z.-D. Qian, Y. Wang, W.-X. Huai, and Y. H. Lee, “Numerical simulation of water flow in an axial flow pump with adjustable guide vanes,” *Journal of Mechanical Science and Technology*, vol. 24, no. 4, pp. 971–976, 2010.




Hindawi

Submit your manuscripts at
<http://www.hindawi.com>

